






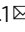



High-efficiency direct methane conversion to oxygenates on a cerium dioxide nanowires supported rhodium single-atom catalyst

Shuxing Bai^{1,6}, Fangfang Liu^{2,6}, Bolong Huang^{3,6} , Fan Li⁴, Haiping Lin² , Tong Wu³, Mingzi Sun³ , Jianbo Wu^{4,5}  , Qi Shao¹, Yong Xu²   & Xiaoqing Huang¹ 

Direct methane conversion (DMC) to high value-added products is of significant importance for the effective utilization of CH₄ to combat the energy crisis. However, there are ongoing challenges in DMC associated with the selective C–H activation of CH₄. The quest for high-efficiency catalysts for this process is limited by the current drawbacks including poor activity and low selectivity. Here we show a cerium dioxide (CeO₂) nanowires supported rhodium (Rh) single-atom (SAs Rh-CeO₂ NWs) that can serve as a high-efficiency catalyst for DMC to oxygenates (i.e., CH₃OH and CH₃OOH) under mild conditions. Compared to Rh/CeO₂ nanowires (Rh clusters) prepared by a conventional wet-impregnation method, CeO₂ nanowires supported Rh single-atom exhibits 6.5 times higher of the oxygenates yield (1231.7 vs. 189.4 mmol g_{Rh}⁻¹ h⁻¹), which largely outperforms that of the reported catalysts in the same class. This work demonstrates a highly efficient DMC process and promotes the research on Rh single-atom catalysts in heterogeneous catalysis.

¹ College of Chemistry, Chemical Engineering and Materials Science, Soochow University, Jiangsu 215123, China. ² Institute of Functional Nano&Soft Materials (FUNSOM), Jiangsu Key Laboratory for Carbon-Based Functional Materials & Devices, Soochow University, Jiangsu 215123, China. ³ Department of Applied Biology and Chemical Technology, The Hong Kong Polytechnic University, Hung Hom, Kowloon, Hong Kong SAR, China. ⁴ State Key Laboratory of Metal Matrix Composites, School of Materials Science and Engineering, Shanghai Jiao Tong University, Shanghai 200240, China. ⁵ Center of Hydrogen Science, Shanghai Jiao Tong University, Shanghai 200240, China. ⁶ These authors contributed equally: Shuxing Bai, Fangfang Liu, Bolong Huang.

email: jjanbowu@sjtu.edu.cn; xuy@suda.edu.cn; hxq006@suda.edu.cn

Methane (CH_4) is in fact among the most important and attractive feedstocks for producing methanol (CH_3OH) and other high value-added products in the chemical industry^{1,2}. In the traditional processes, CH_4 is converted into CH_3OH indirectly via the formation of syngas (H_2 and CO), which is an energy-hungry process that needs to be performed under high temperature^{3,4}. Therefore, the direct CH_4 conversion (DMC) to CH_3OH , which is regarded as a “dream reaction” in chemical industry, has been the subject of intensive study for decades^{5–7}. For instance, Periana et al. reported that CH_4 can be converted to CH_3OH by mercuric ions in the presence of concentrated sulfuric acid⁸. Sushkevich et al.⁹ synthesized a copper-containing zeolite catalyst and used it for the conversion of CH_4 to CH_3OH with high selectivity ($\sim 97\%$) at 200°C . More recently, Agarwal et al. used colloidal gold–palladium nanoparticles (Au–Pd NPs) to catalyze the DMC to CH_3OH , methylhydroperoxide (CH_3OOH), and formic acid (HCOOH) in the presence of hydrogen peroxide (H_2O_2) and oxygen (O_2)¹⁰. The yield of these primary oxygenates product reaches $\sim 53.6 \text{ mol kg}_{\text{cat}}^{-1} \text{ h}^{-1}$ at a selectivity of 88.0% at 50°C ¹⁰. Shan et al.² reported that mononuclear rhodium species on ZSM-5 can catalyze DMC to CH_3OH and acetic acid (CH_3COOH) using O_2 and carbon monoxide (CO) with the total yield of oxygenates $\sim 10 \text{ mmol g}_{\text{cat}}^{-1} \text{ h}^{-1}$ and the selectivity of $\text{CO}_2 \sim 15\%$ ². Despite the tremendous progress on the development of catalysts and technologies, DMC to oxygenates is extremely challenging because the selective activation of C–H bonds in CH_4 under mild conditions is a tough issue. It is thus highly desired to develop active and selective catalysts for the DMC to oxygenates.

Noble metals-based single-atom catalysts (SACs) have emerged as a new frontier in heterogenous catalysis because of large ratio of surface atoms, low-coordination environment of metal centers, and strong metal–support interactions^{11–13}. They have been widely studied in diverse processes with superior catalytic performance, including CO oxidation, CH_4 conversion, oxygen reduction, water gas shift reaction, and so on^{14–16}. Recent investigations show that SACs can be used as highly active and selective catalysts for alkynes hydrogenation, in which the isolated active sites are geometrically in favor of the selective hydrogenation of alkynes^{17–20}. For instance, Kyriakou et al.¹⁷ demonstrated that the isolated Pd atoms in a Cu surface can be used as a highly selective catalyst for the hydrogenation of styrene and acetylene as compared with pure Cu or Pd metal. Yan et al.¹⁸ claimed that Pd SAs can selectively catalyze butadiene to butene because of the mono- π -adsorption mode and the steric effect induced by butadiene adsorption on the isolated Pd atoms. Typical for CH_4 conversion, Tang et al.¹⁵ reported that the single-site Rh_1O_5 anchored in microporous aluminosilicates (ZSM-5) can catalyze the DMC to CH_3COOH and CH_3OH in the presence of CH_4 , CO , and O_2 at $\leq 150^\circ\text{C}$. It is found that the single-site Rh_1O_5 plays the role of the active site for DMC, while the rhodium oxide NPs on ZSM-5 are even not active for this transformation¹⁵. Kwon et al.¹⁶ demonstrated that Rh SA on ZrO_2 can be used for the DMC to CH_3OOH and CH_3OH in H_2O_2 solution at 70°C . However, the selectivity of oxygenates from Rh SA on ZrO_2 is $\sim 70\%$ due to the different decomposition rate of H_2O_2 and CH_3OOH on ZrO_2 ¹⁶. Inspired by these reports, we believe that the Rh SACs can be used as promising catalysts for DMC, and the selectivity of oxygenates may be strongly related to the support for anchoring Rh SA.

Herein, we synthesized Rh-based SACs on CeO_2 nanowires (SAs Rh- CeO_2 NWs) via a simple hydrothermal process. The results show that SAs Rh- CeO_2 NWs can be used as a highly efficient catalyst for DMC to oxygenates in the presence of H_2O_2 at 50°C . Different from the previous work, our work reveals that the support for anchoring Rh SAs (i.e., CeO_2 NWs) is involved in

the formation of radicals, which can further enhance the activity of DMC. The total yield and selectivity of oxygenates reach $\sim 1231.7 \text{ mmol g}_{\text{Rh}}^{-1} \text{ h}^{-1}$ and 93.9%, respectively. To the best of our knowledge, the current DMC performance outperforms the reported catalysts in literatures. In situ characterizations and theoretical calculations show that CeO_2 NWs play a vital role in the formation of $\cdot\text{OOH}$ and $\cdot\text{OH}$ radicals. SAs Rh- CeO_2 NWs can selectively activate CH_4 to $\cdot\text{CH}_3$, which further combines with $\cdot\text{OOH}$ and $\cdot\text{OH}$ radicals to form CH_3OH and CH_3OOH , respectively. By contrast, the Rh/ CeO_2 NWs tend to overoxidize CH_4 to CO_x species with the assistance of $\cdot\text{OH}$, leading to a low oxygenates' yield and selectivity ($189.4 \text{ mmol g}_{\text{Rh}}^{-1} \text{ h}^{-1}$ and 56.4%).

Results

Preparation and morphology characterization. CeO_2 NWs were prepared via a simple hydrothermal process by adding cerium chloride (CeCl_3), sodium oleate, deionized water (H_2O), and *n*-butylamine into a stainless reactor. The synthetic method of SAs Rh- CeO_2 NWs was the same as that of CeO_2 NWs, except for adding additional sodium hexachlororhodate (Na_3RhCl_6). Rh/ CeO_2 NWs and Rh/ CeO_2 -com were prepared by impregnating Na_3RhCl_6 on the as-prepared CeO_2 NWs and commercial CeO_2 via a conventional wet-impregnation method. The physicochemical properties are listed in Supplementary Table 1. Transmission electron microscopy (TEM) image shows that uniform CeO_2 NWs with a diameter and length of $\sim 6.2 \text{ nm}$ and $\sim 260 \text{ nm}$ are obtained (Supplementary Fig. 1). No Rh nanoparticles are observed in TEM image, indicating that Rh atoms are well dispersed in SAs Rh- CeO_2 NWs (Fig. 1a). The aberration-corrected high-angle annular dark-field scanning transmission electron microscopy (AC-HAADF/STEM) image in temperature color of SAs Rh- CeO_2 NWs indicates Rh atoms are presented as SA state (Fig. 1b, c; Supplementary Fig. 2). By contrast, Rh clusters with the size of $\sim 1.5 \text{ nm}$ appear in the AC-HAADF/STEM image in temperature color of Rh/ CeO_2 NWs (Fig. 1d, e; Supplementary Fig. 3). In X-ray diffraction (XRD) pattern of SAs Rh- CeO_2 NWs, only the characteristic peaks of CeO_2 at $2\theta = 28.5, 33.1, 47.5, 56.3, 69.4, 76.7, 79.1, \text{ and } 88.4^\circ$ (PDF No. 43-1002) are observed (Supplementary Fig. 4), indicating that Rh atoms are highly dispersed on CeO_2 NWs and commercial CeO_2 , despite the full wavelength at half maximum (FWHM) of the characteristic peaks corresponding to CeO_2 NWs is much broader than that of commercial CeO_2 due to its small diameter of $\sim 6.2 \text{ nm}$ ²¹. It should be noted that the absence of peaks corresponding to Rh clusters in the XRD pattern of Rh/ CeO_2 NWs might be attributed to the very small-sized Rh clusters and low content of Rh in the catalyst. X-ray photoelectron spectroscopy measurements were performed to characterize the chemical states of elements on the surface of CeO_2 NWs, SAs Rh- CeO_2 NWs, Rh/ CeO_2 NWs, and Rh/ CeO_2 -com. As shown in Supplementary Fig. 5, it is found that Rh are in their oxidation state (Rh^{3+}), while Ce consist of Ce^{4+} (881.8, 888.3, 897.6, 900.3, 907.2, and 916.0 eV) and Ce^{3+} (884.6 and 903.1 eV)²². The binding energy shifts of Rh in XPS spectra indicate that the different synergies among those catalysts. Compared with the Rh/ CeO_2 -com (308.9 eV) and Rh/ CeO_2 NWs (309.1 eV), Rh 3d5/2 peak obviously shifts to 309.4 eV in SAs Rh- CeO_2 NWs, suggesting the existence of electron transfer from Rh to CeO_2 in SAs Rh- CeO_2 NWs (Supplementary Fig. 5a). On the other hand, detailed peak fittings demonstrate that the proportions of Ce^{3+} are different among these samples (Supplementary Fig. 5b). In particular, the proportion of Ce^{3+} in Rh/ CeO_2 -com is 12.4%, which is much lower than that in CeO_2 NWs (16.0%), Rh/ CeO_2 NWs (16.5%), and SAs Rh- CeO_2 NWs (16.7%). XPS results imply a much stronger synergy exists in SAs Rh- CeO_2 NWs in

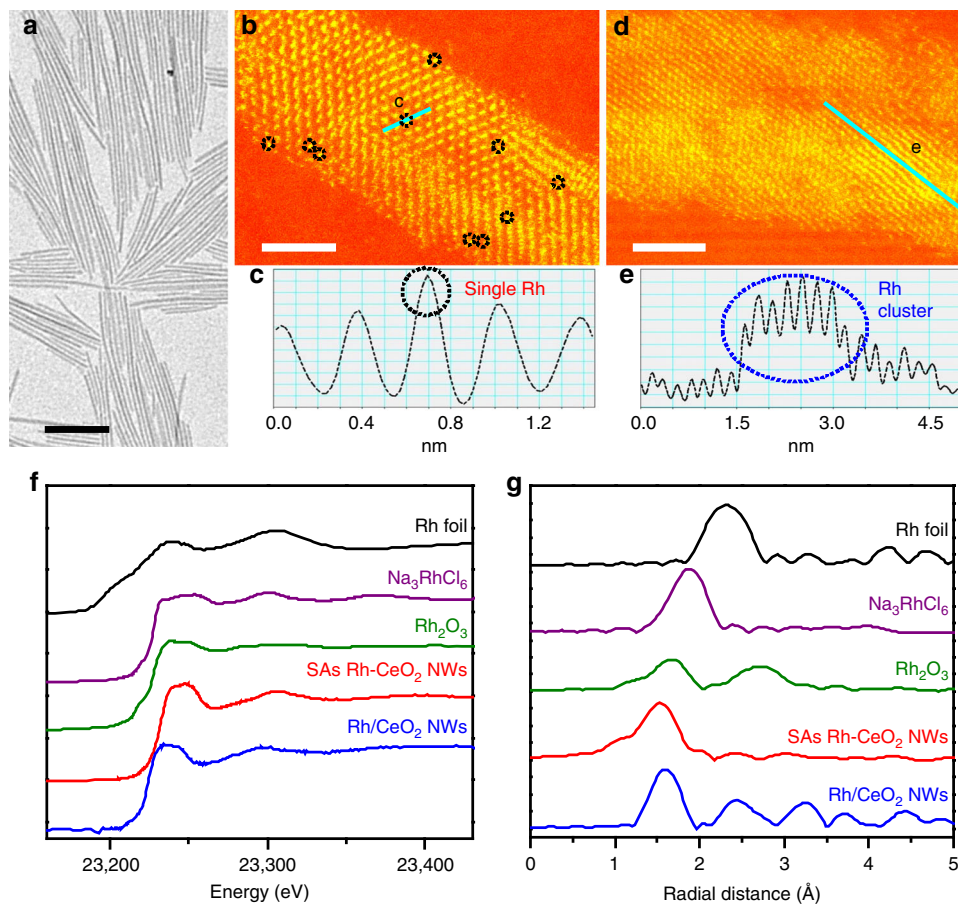


Fig. 1 Structural analyses of SAs Rh-CeO₂ NWs and Rh/CeO₂ NWs. **a** TEM image of the SAs Rh-CeO₂ NWs. **b** AC-HAADF/STEM image in temperature color of the SAs Rh-CeO₂ NWs. The isolated Rh atoms are marked with black circles. **c** The intensity profile recorded from the line in panel (**b**). **d** AC-HAADF/STEM image in temperature color of the Rh/CeO₂ NWs. The Rh cluster is marked with blue line. **e** The intensity profile recorded from the line in panel (**d**). **f, g** Rh K-edge XANES spectra (**f**) and Rh K-edge EXAFS spectra in *R* space (**g**) of the Rh foil, Na₃RhCl₆, Rh₂O₃, SAs Rh-CeO₂ NWs, and Rh/CeO₂ NWs. The scale bars in (**a**), (**b**), and (**d**) are 100, 2, and 2 nm, respectively.

comparison with Rh/CeO₂ NWs and Rh/CeO₂-com. No obvious peaks in Na 1s and Cl 2p XPS spectra suggest that neglect amount of Na and Cl remain on catalysts (Supplementary Fig. 5c, d).

To study the electronic structures and coordination states of Rh in the SAs Rh-CeO₂ NWs and the Rh/CeO₂ NWs, X-ray absorption near-edge spectroscopy (XANES) and extended X-ray fine structure (EXAFS) were measured at Rh K-edge. Rh foil, Rh₂O₃, and Na₃RhCl₆ were used as references. Comparing with the edge position in the XANES spectra of references, Rh in SAs Rh-CeO₂ NWs and Rh/CeO₂ NWs are presented as their oxidation states (Fig. 1f). As shown in Fig. 1g, the Rh–Rh coordination, Rh–Cl coordination, Rh–O, and the second shell of Rh–O coordination are observed at ~2.3 Å, ~1.9 Å, ~1.7 Å, and ~2.7 Å, respectively¹⁵. For Rh/CeO₂ NWs, Rh–O, and Rh–Rh coordination appear at ~1.6 Å and ~2.4 Å in the *R*-space EXAFS spectrum, indicating the presence of Rh clusters in Rh/CeO₂ NWs. By contrast, only the feature of Rh–O coordination at ~1.6 Å is observed in the *R*-space spectrum of SAs Rh-CeO₂ NWs (Fig. 1g). The disappearance of Rh–Rh coordination implies that Rh atoms in SAs Rh-CeO₂ NWs are presented as isolated atoms, which is in good agreement with the observations in AC-HAADF/STEM image^{16,23}. It is noted that no obvious Rh–Cl coordination is observed in the EXAFS spectrum of SAs Rh-CeO₂ NWs, indicating that the Rh atoms are anchored by O atoms in CeO₂ NWs via Rh–O coordination. In addition, the structures of SAs Rh-CeO₂ NWs and Rh/CeO₂ NWs were verified by the diffuse reflectance-infrared Fourier transform spectroscopy (DRIFTS)

measurement using CO as a probe. As shown in Supplementary Fig. 6a, different from the previous reports that Rh SA gives geminal peaks in 2000–2100 cm⁻¹, only one broad and weak peak is observed at 2000–2150 cm⁻¹ in the CO-DRIFTS spectrum of SAs Rh-CeO₂ NWs, which may be attributed to the low CO coverage on SAs Rh-CeO₂ NWs²⁴. The presence of oxidation species at 1250–1700 cm⁻¹ indicates that the adsorbed CO molecules are oxidized, further confirming the low CO coverage on the surface of SAs Rh-CeO₂ NWs. When SAs Rh-CeO₂ NWs was pretreated in CO at 50 °C for 0.5 h, the intensity of peak at 2000–2150 cm⁻¹ obviously increases, despite the appearance of oxidation species. Further increasing the pretreatment temperature to 150 °C, two intense peaks appear at 2101 and 2030 cm⁻¹ in CO-DRIFTS spectrum of SAs Rh-CeO₂ NWs, which correspond to the symmetric and asymmetric vibration of gem-dicarbonyl doublet CO (i.e., Rh(CO)₂) (Supplementary Fig. 6a, red curve)²⁵. For Rh/CeO₂ NWs, in addition to the peaks of oxidation species, multiple peaks corresponding to the symmetric (2101 cm⁻¹) and asymmetric vibration (2030 cm⁻¹) of Rh(CO)₂ and CO linear adsorption on Rh^{δ+} (2133 cm⁻¹) are observed in CO-DRIFTS spectrum (Supplementary Fig. 6b). When Rh/CeO₂ NWs was pretreated at 50 °C and then 150 °C for 0.5 h, two peaks appear at 1860 and 2060 cm⁻¹ in CO-DRIFTS spectrum, which correspond to the CO bridge adsorption and linear adsorption on Rh, respectively (Supplementary Fig. 6b, red curve)^{24,25}. The absence of CO bridge adsorption in the CO-DRIFTS spectrum further confirms the structures of Rh SA in SAs

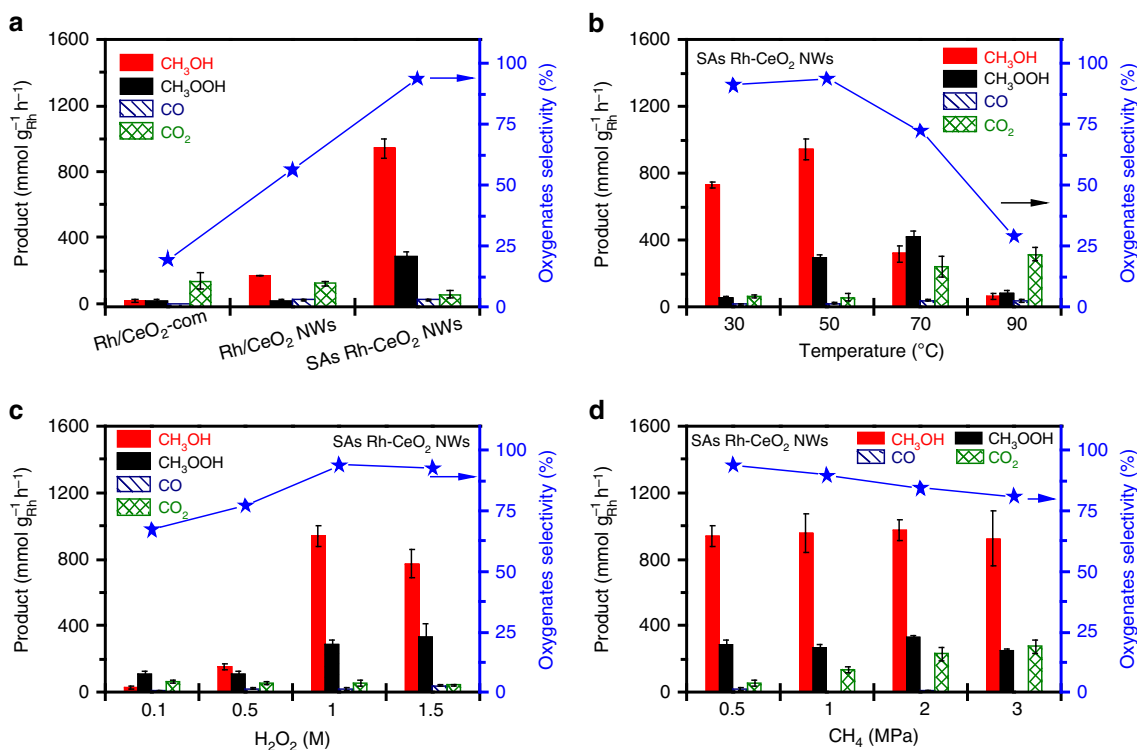


Fig. 2 DMC performance on different catalysts. **a** The yield and selectivity of oxygenates from Rh/CeO₂-com, Rh/CeO₂ NWs, and SAs Rh-CeO₂ NWs. Reaction conditions: P_{CH_4} : 0.5 MPa, H₂O₂: 20 mL (1 M), T : 50 °C, reaction time: 1 h, and catalyst weight: 10 mg. **b** DMC performance at different temperatures over SAs Rh-CeO₂ NWs. Reaction conditions: P_{CH_4} : 0.5 MPa, H₂O₂: 20 mL (1 M), T : 30–90 °C, reaction time: 1 h, and catalyst weight: 10 mg. **c** DMC performance at different H₂O₂ concentrations over SAs Rh-CeO₂ NWs. Reaction conditions: P_{CH_4} : 0.5 MPa, H₂O₂: 20 mL (0.1–1.5 M), T : 50 °C, reaction time: 1 h, and catalyst weight: 10 mg. **d** DMC performance at different CH₄ partial pressure over SAs Rh-CeO₂ NWs. Reaction conditions: P_{CH_4} : 0.5–3 MPa, H₂O₂: 20 mL (1 M), T : 50 °C, reaction time: 1 h, and catalyst weight: 10 mg. The error bars are defined as standard deviation of three experiments.

Rh-CeO₂ NWs, which is in good agreement with the result of AC-HAADF/STEM and X-ray absorption spectroscopy²⁵.

DMC performance of SAs Rh-CeO₂ NWs and Rh/CeO₂ NWs.

All the catalysts of Rh/CeO₂-com, Rh/CeO₂ NWs, and SAs Rh-CeO₂ NWs were used for DMC in a pressurized reactor. Products were analyzed by gas chromatography and ¹H nuclear magnetic resonance spectroscopy (¹H-NMR). As shown in Fig. 2a, Rh/CeO₂-com gives the CH₃OH, CH₃OOH, and CO_x yield of 17.6, 15.6, and 137.4 mmol g_{Rh}⁻¹ h⁻¹, respectively. When Rh/CeO₂ NWs are used as a catalyst, the yield of CH₃OH and CH₃OOH increase to 170.4 mmol g_{Rh}⁻¹ h⁻¹ and 19.0 mmol g_{Rh}⁻¹ h⁻¹, respectively, while the total yield of CO_x is 146.3 mmol g_{Rh}⁻¹ h⁻¹. The low selectivities of oxygenate on Rh/CeO₂-com (19.5%) and Rh/CeO₂ NWs (56.4%) indicate that CH₄ tends to be overoxidized into CO_x on Rh/CeO₂-com and Rh/CeO₂ NWs. By contrast, when SAs Rh-CeO₂ NWs are used as a catalyst, the selectivity of CO_x significantly decreases to 6.1%, indicating that the overoxidation of CH₄ is strongly suppressed on SAs Rh-CeO₂ NWs. Correspondingly, the yield of CH₃OH and CH₃OOH significantly increase to 940.3 and 291.4 mmol g_{Rh}⁻¹ h⁻¹, respectively. Moreover, SAs Rh-CeO₂ NWs were tested for DMC under different conditions (i.e., temperature, H₂O₂ concentration, CH₄ pressure, and catalysts amount). As depicted in Fig. 2b, it is found that the increase of temperature leads to a volcano-shape selectivity and yield of oxygenates. Typically, the selectivity and yield of oxygenates are 91.4% and 786.3 mmol g_{Rh}⁻¹ h⁻¹ at 30 °C, which further increases to 93.9% and 1231.7 mmol g_{Rh}⁻¹ h⁻¹ at 50 °C. Further increase in temperature will lead to a decrease in

both the selectivity and yield of oxygenates. A similar tendency is observed when the concentration of H₂O₂ is increased from 0.1 to 1.5 M (Fig. 2c). For instance, the selectivity and yield of oxygenates are 67.1% and 145.0 mmol g_{Rh}⁻¹ h⁻¹ at the H₂O₂ concentration of 0.1 M, which significantly increase to 93.9% and 1231.7 mmol g_{Rh}⁻¹ h⁻¹ at the H₂O₂ concentration of 1.0 M, indicating H₂O₂ can significantly promote the DMC activity. It is noted that a further increase of H₂O₂ concentration to 1.5 M will result in a slight decay in oxygenates selectivity and yield. Furthermore, the effects of CH₄ partial pressure on DMC performance were studied. As shown in Fig. 2d, the selectivity of CO_x strongly increases from 6.1% to 21.1% when the CH₄ partial pressure is increased from 0.5 MPa to 3 MPa, despite the similar yield of oxygenates. We thus further tested the DMC performance by altering the weight of the catalyst, as shown in Supplementary Fig. 7. It is found that the yield of CH₃OH and CH₃OOH steadily increase as the increasing weight of catalyst, while the selectivity of CH₃OH and CH₃OOH are kept at ~94%. The positive effects of H₂O₂ concentration and catalyst weight but negligible effects of CH₄ partial pressure on the oxygenates selectivity imply that Rh SA can efficiently activate C–H bonds in CH₄ under the optimized conditions, and the rate-determining steps solely involve the reaction of CH₄ activation intermediates with H₂O₂ (Fig. 2; Supplementary Fig. 7)¹⁰. In addition, SAs Rh-CeO₂ NWs were used in ten consecutive DMC cycles to test the stability. As shown in Supplementary Fig. 8, no obvious decays in oxygenates selectivity and yield are observed after ten consecutive DMC cycles. The structures of Rh SA are reserved in the spent SAs Rh-CeO₂ NWs, indicating that SAs Rh-CeO₂ NWs can be used as a stable catalyst for DMC (Supplementary Fig. 9). Moreover, to the best of

our knowledge, the current DMC performance has outperformed the reported catalysts (Supplementary Table 2), suggesting that SAs Rh-CeO₂ NWs can be used as a highly efficient catalyst for DMC to oxygenates under mild conditions.

Mechanistic studies on DMC. In order to study the mechanism of CH₄ selective oxidation on SAs Rh-CeO₂ NWs, DMC was performed using O₂ as the oxidant to replace H₂O₂. As depicted in Supplementary Table 3, the selectivity of oxygenates is 5.9% when O₂ is solely used as the oxidant, which significantly increases to 92.8% after the addition of 10 μmol H₂O₂. Correspondingly, the yield of oxygenates increases from 17.6 to 1159.4 mmol g_{Rh}⁻¹ h⁻¹, indicating that H₂O₂ can significantly promote DMC to oxygenates. Based on the previous reports¹⁰, we speculated that the DMC in the presence of H₂O₂ might follow radical-triggered reaction paths. Therefore, electron paramagnetic resonance (EPR) was performed to detect the radicals in the present reaction system by using 5,5'-dimethyl-1-pyrroline-N-oxide (DMPO) as the radical scavenger. In order to label the radicals, two contrast experiments were performed in the systems of DMPO + H₂O₂ + Fe²⁺ and DMPO + H₂O₂ + Fe²⁺ + CH₃OH (detailed information has been given in the experimental section). As shown in Supplementary Fig. 10, a four-line EPR spectrum with a relative peak ratio of 1:2:2:1 is obtained from the DMPO + H₂O₂ + Fe²⁺ system (Supplementary Fig. 10, green curve), which can be assigned to ·OH radical²⁶. For the system of DMPO + H₂O₂ + Fe²⁺ + CH₃OH, a six-line EPR spectrum is recorded, which can be indexed as the characteristic peaks of ·CH₃ radical (Supplementary Fig. 10, blue curve)²⁶. When DMPO is added into the reaction system, some new peaks of ·OOH appear in the EPR spectrum in addition to those peaks of ·CH₃ and ·OH radicals (Supplementary Fig. 10, red curve)²⁷. The presence of ·CH₃, ·OOH, and ·OH radicals in the reaction system further confirms that the DMC on the SAs Rh-CeO₂ NWs in H₂O₂ solution is triggered by radicals.

To further study the working mechanism of the radical-triggered DMC on SAs Rh-CeO₂ NWs, in situ DRIFTS measurements were performed to analyze the surface species on SAs Rh-CeO₂ NWs and Rh/CeO₂ NWs when they were exposed to H₂O₂ and CH₄. First, we exposed SAs Rh-CeO₂ NWs and Rh/CeO₂ NWs into H₂O₂. As shown in Supplementary Fig. 11, three intense peaks are observed at 3401, 3214, and 1654 cm⁻¹ in the spectra of SAs Rh-CeO₂ NWs and Rh/CeO₂ NWs, which can be assigned to *OH, *OOH, and *OH₂, respectively²⁸. Based on the observations in EPR spectra (Supplementary Fig. 10) and previous reports, we conclude that H₂O₂ can decompose into active radicals on CeO₂ NWs^{29,30}. When the SAs Rh-CeO₂ NWs are exposed to CH₄, the characteristic bands of *CH₃ appear at 1412 and 1304 cm⁻¹ (see ref. ³¹), indicating that SAs Rh-CeO₂ NWs can selectively activate CH₄ into *CH₃ (Fig. 3a, black curve). Moreover, two additional bands are observed at 1635 and 3401 cm⁻¹, which can be ascribed as *OH₂ and *OH, respectively, suggesting that *OH may combine with H from CH₄ decomposition to form *OH₂. When SAs Rh-CeO₂ NWs are exposed to the mixture of CH₄ and H₂O₂ (Fig. 3a, red curve), new peaks appear at 2935, 2837, 1438, 1353, 1220, and 1148 cm⁻¹ in the spectrum, which can be assigned to the C–H asymmetric stretching vibration, C–H symmetric stretching vibration, CH₃ scissoring vibration, CH₃ asymmetric rocking vibration, C–O stretching vibration and CH₃ symmetric rocking vibration of *OCH₃, respectively^{32,33}. The appearance of *OCH₃, *OH, and *OOH demonstrates the formation of CH₃OH and CH₃OOH. By contrast, when Rh/CeO₂ NWs are exposed to CH₄, only two strong bands of CO₃²⁻ and *CO₂^{δ-} are observed at 1589 and 1293 cm⁻¹ (Fig. 3b, black spectrum)³⁴. The absence of *CH₃,

*OH, and *OH₂ suggests that CH₄ is overoxidized into CO_x species. When Rh/CeO₂ NWs are exposed to the mixture of CH₄ and H₂O₂, the intense band of CO₃²⁻ in the spectrum implies that CO_x are the dominant products despite the appearance of *OCH₃ and *OH bands (Fig. 3b, blue curve)³⁵, which is consistent with our experimental results (Fig. 2a).

To further confirm the activation of CH₄ on Rh, CH₄ temperature programmed surface reaction (TPSR) was performed to investigate the CH₄ conversion on CeO₂ NWs, SAs Rh-CeO₂ NWs, and Rh/CeO₂ NWs. No obvious peaks are observed in the TPSR pattern of CeO₂ NWs, suggesting that CeO₂ NWs are inactive for CH₄ activation under the indicated conditions (Supplementary Fig. 12). When CH₄-TPSR measurements were performed on SAs Rh-CeO₂ NWs and Rh/CeO₂ NWs, the peaks of CH₄, CO, CO₂, and H₂O appear in TPSR patterns, suggesting that Rh atoms play as the active sites for CH₄ activation (Fig. 3c, d), which is in good agreement with results from the in situ DRIFTS measurement (Fig. 3a, b). Despite the appearance of peaks in TPSR patterns, the different onset temperatures (*T*_{onset}) suggest that the reaction paths are different on SAs Rh-CeO₂ NWs and Rh/CeO₂ NWs (Fig. 3c, d). For SAs Rh-CeO₂ NWs, the *T*_{onset} of CH₄ (~82 °C, formed via *CH₃ hydrogenation) is closed to that of CO (~82 °C) and CO₂ (~82 °C), indicating that *CH₃ hydrogenation (to form CH₄) and overdehydrogenation (to form CO_x) competitively occur on the SAs Rh-CeO₂ NWs. By contrast, the *T*_{onset} of CO₂ (~67 °C) and CO (~61 °C) is significantly lower than that of CH₄ (~74 °C) in TPSR patterns of Rh/CeO₂ NWs, indicating that overoxidation for the formation of CO and CO₂ is preferential⁵.

DFT calculations. Finally, DFT calculations were performed to reveal the reaction paths of CH₄ oxidation on SAs Rh-CeO₂ NWs and Rh/CeO₂ NWs. The real spatial orbital distribution apparently shows the concentrated electron-rich feature on SAs Rh, which indicates the Rh site possesses a superior reaction priority among the available sites on the surface. Meanwhile, Rh cluster on CeO₂ shows widely separated electronic distribution over the surface, which shows the disperse electroactive region (Fig. 4a). The projected density of states (PDOS) support that the highly concentrated electronic activity of SAs Rh on the surfaces is attributed to the sharp Rh-4d occupation near the Fermi level (*E*_F). The Ce-4f bands mainly locate above *E*_F, while O-2p bands concentrate on *E*_v - 4.5 eV. The evident coupling between Rh-4d and Ce-4d confirms the stabilization of SAs Rh by the protection of bottom Ce (Fig. 4b). In comparison, the Rh-4d bands become much broad in Rh/CeO₂, covering from *E*_v - 5.0 eV to *E*_v + 2.0 eV. The evident match among Rh-4d bands and O-2p bands and Ce-4f bands indicates a strong coupling between the surface Rh cluster and bottom CeO₂ (Fig. 4c). The electronic structures of CH₄ adsorption are further presented to illustrate the different activity toward the DMC process. It is noted the dominant peak of Rh-4d in SAs Rh-CeO₂ upshifts from *E*_v - 2.0 eV toward *E*_v - 1.0 eV due to the electron transfer with CH₄ (Fig. 4d). Meanwhile, the close distance between Rh-4d bands and O-2p bands on Rh/CeO₂ NWs demonstrates the strong couplings between CH₄ and local O atoms, which lead to the over-binding effect with increased energy barriers for the consecutive dehydrogenation of CH₄ (Fig. 4e).

Since EPR and in situ DRIFTS results show that lattice O atoms of CeO₂ are feasibly bonded with H in H₂O₂. From the energetic view, DFT also proves the superior flexibility of O in SAs Rh-CeO₂ NWs with only 0.16 eV energy barrier. Due to the steric hindrance from the surface coverage of Rh cluster, the energy barrier of the detachment of O in Rh/CeO₂ NWs increases to 4.06 eV, demonstrating a slow efficiency of generating ·OOH

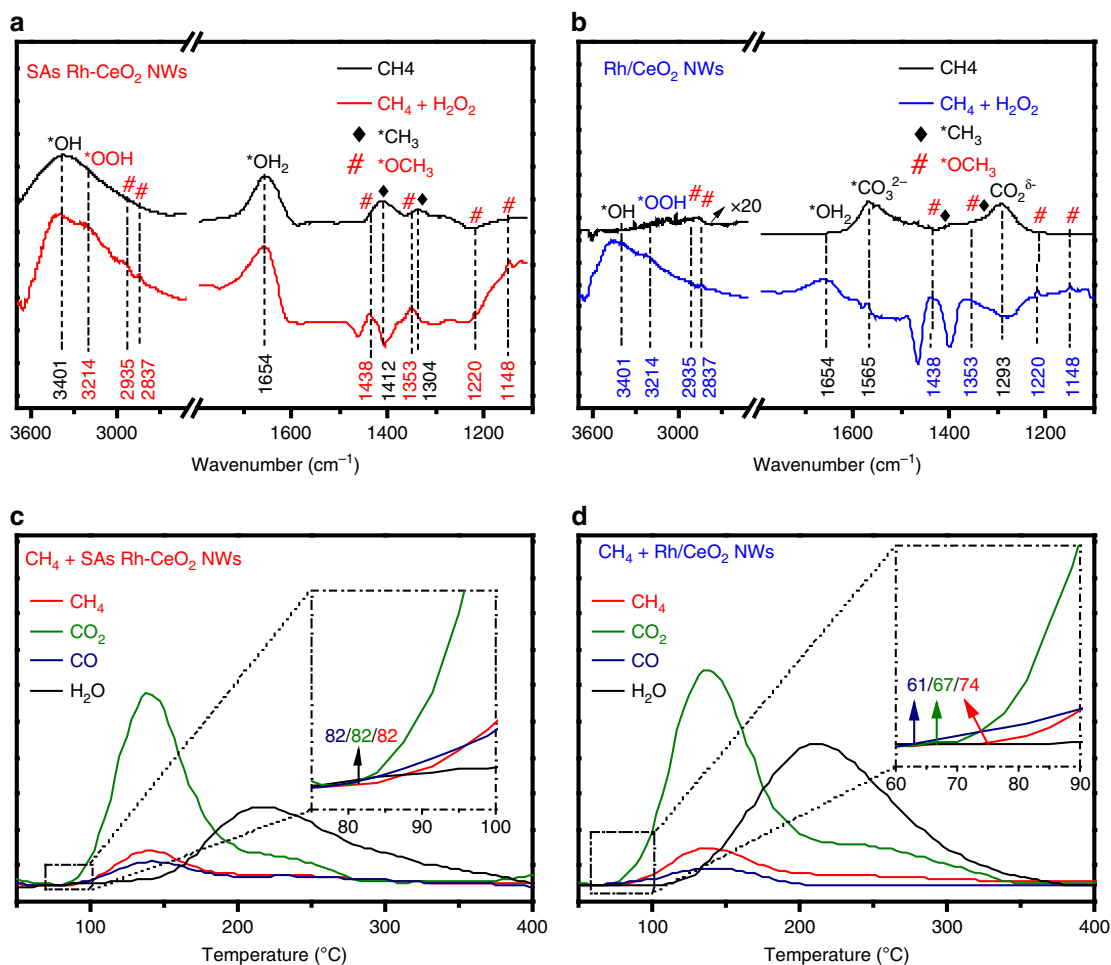


Fig. 3 In situ CH₄-DRIFTS and CH₄-TPSR measurement. **a, b** In situ CH₄-DRIFTS measurements on SAs Rh-CeO₂ NWs (**a**) and Rh/CeO₂ NWs (**b**). **c, d** CH₄-TPSR measurements on SAs Rh-CeO₂ NWs (**c**) and Rh/CeO₂ NWs (**d**).

radicals (Fig. 4f). The further reaction energies also support that the generations of both ·OH and ·OOH radicals are much more preferred in SAs Rh-CeO₂ NWs, satisfying the prerequisite of radical-mediated DMC process (Fig. 4g). The SAs Rh-CeO₂ NWs deliver an overall downhill trend to the formation final product CH₃OH and CH₃OOH, representing a high electronic activity. The spontaneous adsorption of CH₄ and facile C–H bond cleavage indicates the fast activation of C–H bond, which leads to the efficient DMC process. Particularly, the further reaction of CH₃OOH toward HCOOH has been suppressed by the high energetic barrier of 1 eV, guaranteeing the reaction locking for desired products. The formation of CH₃OH releases 2.87 eV, which is slightly larger energy than that of CH₃OOH (2.53 eV), explaining the higher yield of oxygenates in our experiments. Meanwhile, the high energy cost (2.01 eV) to achieve further C–H bond cleavage of CH₃ facilitates the high selectivity of DMC on the SAs Rh-CeO₂ NWs (Fig. 4h). In contrast, the activation of C–H bond in CH₄ faces stepped energy barriers toward *CH₂ on Rh/CeO₂ NWs, indicating a much lower selectivity of oxygenates. The formation of CH₃OOH induced by the ·OOH radical requires an energy cost of 0.47 eV, while the generation of CH₃OH is energetically favorable. Notably, both *CH₂ and CH₃OOH exhibit an evident energy drop toward the formation of HCOOH, indicating that the overoxidation of CH₄ is preferred. However, the further oxidation of HCOOH to CO shows an energy barrier of 2.08 eV, which further lowers the DMC efficiency. The overall energy release is 1.92 eV, which is much

smaller than that of SAs Rh-CeO₂ NWs, supporting the stronger reaction activity of SAs Rh-CeO₂ NWs toward the DMC conversion (Fig. 4i).

Reaction pathways. Combining the results from EPR, in situ DRIFTS and DFT calculations, we thus summarized the reaction paths of DMC on the SAs Rh-CeO₂ NWs and Rh/CeO₂ NWs (Supplementary Figs. 13 and 14). As displayed in Supplementary Fig. 13, for the SAs Rh-CeO₂ NWs, H₂O₂ can decompose into ·OH on two neighboring Ce (III) atoms (step 1). On the other hand, H₂O₂ can decompose into ·OOH on Ce (IV), and the remaining ·H will combine with [O] (lattice O of CeO₂) connected with the Ce (IV) in CeO₂ NWs to form ·[O]H (step 2). The adsorbed CH₄ on Rh SA can be oxidized into ·CH₃ and H₂O with the assistance of ·OH (step 3). As a result, the formed ·CH₃ will react with the ·OOH and ·[O]H radicals to produce CH₃OOH and CH₃[O]H via steps 4 and 5. It should be noted that the lattice [O] in CeO₂ NWs will be compensated by H₂O₂ (Ce (III) → Ce (IV)). By contrast, the reaction paths are different on the Rh/CeO₂ NWs, despite the paths of H₂O₂ decomposition (steps 1–2) are the same (Supplementary Fig. 14). On Ru clusters, CH₄ can be activated into ·CH₃ by ·OH, which may (i) react with ·[O]H to CH₃[O]H (step 4), or (ii) combine with ·OOH to produce CH₃OOH (step 5), or (iii) be further oxidized into *CH₂ by ·OH (step 6). Both the CH₃OOH and *CH₂ will be converted into *CH₂O (steps 7 and 8) and then to *HCOOH on the Rh/CeO₂

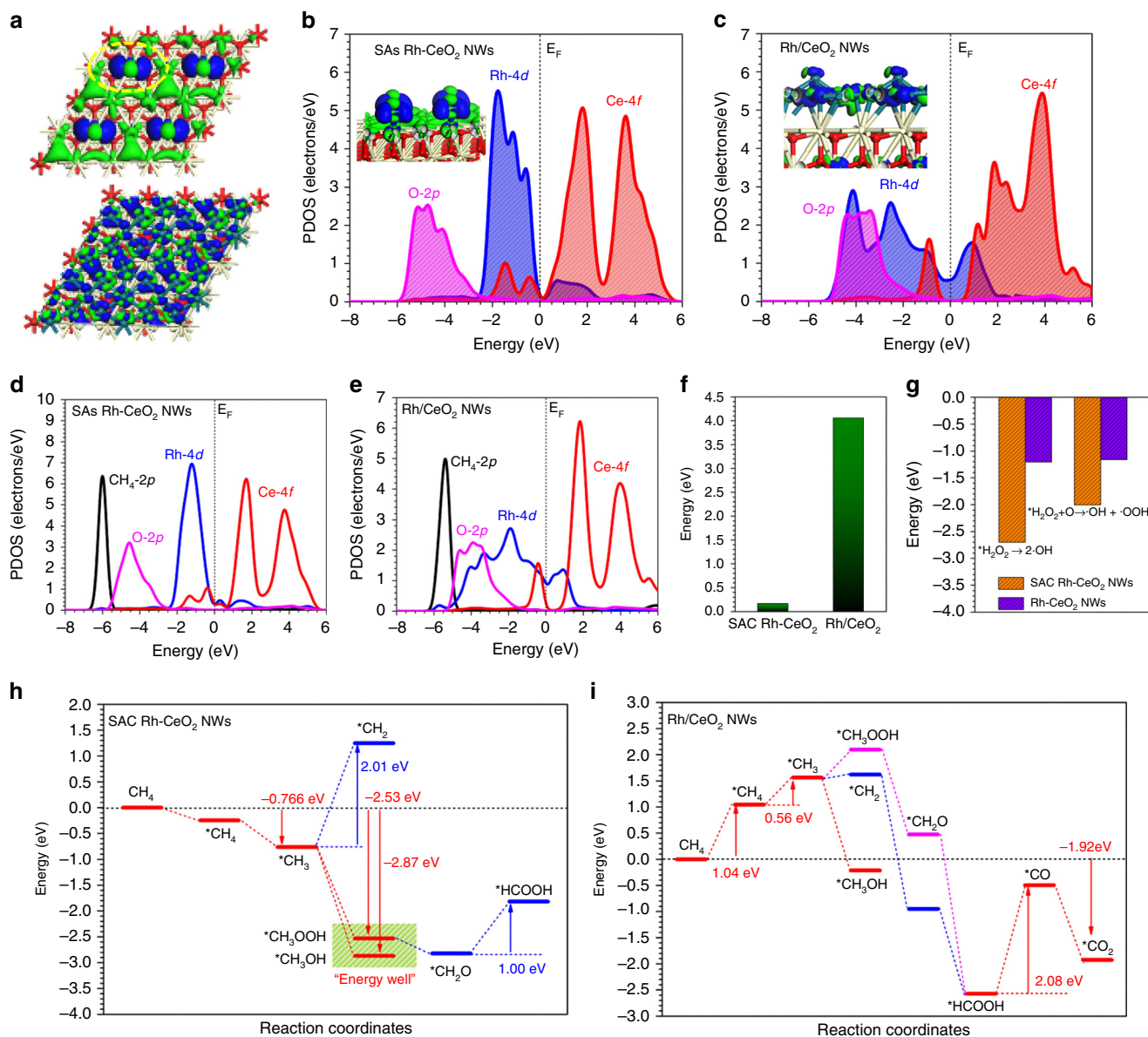


Fig. 4 DFT calculations of DMC reaction paths on SACs Rh-CeO₂ NWs and Rh/CeO₂ NWs. **a** The real spatial contour plots for bonding and antibonding orbitals near E_F for SACs Rh-CeO₂ NWs and Rh/CeO₂ NWs. **b** The PDOS of SACs Rh-CeO₂ NWs surface. **c** The PDOS of Rh/CeO₂ NWs surface. **d** The PDOS of CH₄ adsorption on SACs Rh-CeO₂ NWs surface. **e** The PDOS of CH₄ adsorption on Rh/CeO₂ NWs surface. **f** Energy comparison of [O] desorption from CeO₂ on SACs Rh-CeO₂ NWs and Rh/CeO₂ NWs. **g** The reaction energy comparison of generating radicals. **h** Reaction paths and energy profile of DMC over SACs Rh-CeO₂ NWs. **i** Reaction paths and energy profile of DMC over the Rh/CeO₂ NWs.

NWs (step 9). Finally, HCOOH will be further oxidized into CO_x in the presence of ·OH (steps 10–11).

Discussion

In summary, we demonstrated that SACs Rh-CeO₂ NWs can be used for DMC to oxygenates. Compared with the low selectivity (56.4%) and yield (189.4 mmol g_{Rh}⁻¹ h⁻¹) of oxygenates from Rh/CeO₂ NWs, the selectivity and yield of CH₃OH and CH₃OOH are 93.9% and 1231.7 mmol g_{Rh}⁻¹ h⁻¹ on SACs Rh-CeO₂ NWs at 50 °C, which to the best of our knowledge outperforms the reported values in the literatures. In situ characterizations and experiments were performed to study the mechanism. It is shown that CeO₂ NWs play a vital role in the generation of ·OH and ·OOH radicals, which can significantly promote the oxidation of CH₄ via different reaction paths. To be more specific, SACs Rh-CeO₂ NWs can selectively activate CH₄ to *CH₃, leading to the

formation of oxygenate in the presence of H₂O₂, while Rh/CeO₂ NWs favor the overoxidation of CH₄ to form CO_x, leading to a low selectivity and yield of oxygenates. DFT calculations reveal the facile C–H bond activation and reaction locking on SACs Rh-CeO₂ NWs guarantees the high selectivity and yield of DMC, supplying solid evidence for experimental results. This work may not only provide a highly active and selective catalyst for DMC to oxygenate but also promote the researches of SACs in heterogeneous catalysis.

Methods

Preparation of CeO₂ nanowires (NWs) and SACs Rh-CeO₂ NWs. In a typical preparation of CeO₂ NWs, 12 mL CeCl₃ (0.5 mmol, Alfa Aesar) and sodium oleate (0.75 mmol, Tokyo Chemical Industry) aqueous solution were added into a 20-mL Teflon-lined stainless-steel autoclave. The mixture was magnetically stirred at 800 rpm (round per minute) for 0.5 h. To this solution, *n*-butylamine (1 mL, Sino-pharm) was slowly added into the solution under stirring for another 0.5 h.

Afterward, the autoclave was heated at 160 °C for 10 h before it was cooled to room temperature. The resulting products were collected by centrifugation and washed three times with cyclohexane/acetone mixture, and then dried at room temperature overnight. The powder products were subjected to thermal annealing in an air atmosphere at 400 °C for 10 min at a heating rate of 10 °C min⁻¹. For SAs Rh-CeO₂ NWs, all the parameters were the same with CeO₂ NWs, except for adding extra Na₃RhCl₆ (5 μmol, Aldrich).

Preparation of Rh/CeO₂ NWs and Rh/CeO₂-com. The Rh/CeO₂ NWs and Rh/CeO₂-com were prepared via a conventional wet-impregnation method. Typically, a certain amount of Na₃RhCl₆ solution was dropwise added into the as-prepared CeO₂ NWs and commercial CeO₂ (99.9%, Inoke) under moderate stirring. The resultant slurry was mixed evenly and then dried in an oven at 80 °C overnight, and then subjected to thermal annealing in air at 400 °C for 10 min at a heating rate of 10 °C min⁻¹. Finally, the calcinated samples were re-washed water for three times via centrifugation, and then dried at 100 °C overnight.

Characterization. The morphologies and sizes of the NWs were determined by TEM (Hitachi, HT7700) at 120 kV. AC-HAADF-STEM images were taken on JEM-ARM200F with a cold-field emission gun and a spherical aberration corrector. The Rh loading amounts were determined by the inductively coupled plasma atomic emission spectroscopy (ICP-AES) (710-ES, Varian). XRD patterns were collected on X'Pert-Pro MPD diffractometer (Netherlands PANalytical) with a Cu Kα X-ray source (λ = 1.540598 Å). XPS was done with an SSI S-Probe XPS Spectrometer. The carbon peak at 284.6 eV was used as a reference to correct for charging effects. The X-ray absorption data at the Rh K-edge of the samples were recorded at room temperature in transmission mode using ion chambers at beamline BL14W1 of the Shanghai Synchrotron Radiation Facility (SSRF), China. The station was operated with a Si (311) double-crystal monochromator. During the measurement, the synchrotron was operated at energy of 3.5 GeV and a current between 150 and 210 mA. The photon energy was calibrated with the first inflection point of Rh K-edge in Rh metal foil.

Typical process for selective oxidation of CH₄. The selective oxidation of CH₄ was performed in a 60-mL stainless-steel autoclave. Typically, 20 mL H₂O₂ solution (1 M) and 10 mg of catalyst were added into a Teflon inlet. Afterward, the autoclave was pressurized with CH₄ (0.5 MPa). The reaction was performed at 50 °C with stirring at 800 rpm for 1 h. In our work, we used a commercial Agilent GC integrated system with a flame ionization detector (FID) for the detection of gaseous products. This system contains three columns (two hayesep Q columns and one 5 A mol sieve column) for the separation of gaseous products. Both CO and CO₂ were converted into CH₄ via a methanator to analyze by FID. All the gaseous products were introduced into two tandem hayesep Q columns for pre-separation. CO₂ was completely separated in this process and introduced into the FID via a switch valve. The remaining gases were further introduced into a 5 A mol sieve column for further separation. ¹H nuclear magnetic resonance spectroscopy (¹H-NMR, Bruker 600 MHz) was employed for structural analysis of liquid products, in which dimethylsulfoxide (DMSO, 1%) and deuterioxide were used as the internal standard and solvent, respectively. The liquid products were analyzed by a gas chromatograph (Persee G5) with a FID using a KB-5 column. In total, 10 μL of isopropanol/H₂O (1%) was used as the internal standard adding into 1 mL reaction mixture for analyzing CH₃OH and CH₃OOH. The amount of CH₃OH was calculated using the standard curve method. Afterward, CH₃OOH was converted to CH₃OH using hydrazine hydrate (0.1 mL). The total amount of CH₃OH and CH₃OOH were analyzed by gas chromatograph, and the amount of CH₃OOH was obtained by minusing. For each catalytic test, error bar was obtained by repeating three times. The yields of products and the selectivity were calculated using Eqs. (1) and (2).

$$\text{Yields of products (mmol g}_{\text{Rh}}^{-1} \text{ h}^{-1}) = \text{mmol of products/g of Rh/h of reaction time} \quad (1)$$

$$\text{Oxygenates selectivity (\%)} = \frac{\text{mmol of (CH}_3\text{OOH} + \text{CH}_3\text{OH)}}{\text{mmol of all products}} \times 100 \quad (2)$$

EPR measurement. The detection of free radicals in the reaction process of DMC was performed at a JEOL JES-FA200 electron paramagnetic resonance spectroscopy (EPR, 9.062 GHz), using DMPO as the scavenger. Typically, 1 mL DMPO-H₂O (100 mmol L⁻¹) was added into 1 mL of reaction mixture. The mixed solution was immediately transferred to a capillary tube (diameter: 0.1 mm; filling liquid height: ~5 cm), which was then fixed in the resonant cavity of the spectrometer. EPR measurements were detected at room temperature and recorded by three scans. The contrast experiments were performed to determine the type of radicals by characteristic peaks. Contrast experiment 1 (labeled as DMPO + H₂O₂ + Fe²⁺): 1 mL ferrous (II) sulfate (FeSO₄, 50 mmol L⁻¹) and nitric acid solution (pH = 4) were mixed with 1 mL DMPO-H₂O (100 mmol L⁻¹) under moderate stirring for 2 min, followed by adding 50 μL of H₂O₂ (30 wt.%). Contrast experiment 2 (labeled as DMPO + H₂O₂ + Fe²⁺ + CH₃OH): all the processes were the same with

contrast experiment 1, except for the addition of 1 mL of CH₃OH (100 mmol L⁻¹) into the solution.

CO-DRIFTS measurement. In all, 20 mg sample was packed into a Harrick Praying Mantis high-temperature reaction chamber (CaF₂ windows) mounted inside of a Thermo Scientific Praying Mantis diffuse reflectance adapter, set inside of a Thermo Scientific Nicolet 6700 Fourier transform infrared (FT-IR) spectrometer using liquid nitrogen cooled mercury-cadmium-telluride detector (MCT). Gases were flowed to the reaction chamber using Alicat mass flow controllers. Prior to CO-DRIFTS measurement, the sample was pretreated by heating in CO/Ar (10 vol.%) flow (50 mL min⁻¹) at different temperatures (e.g., -30 °C, 50 °C, and 150 °C), followed by flushing with Ar flow (50 mL min⁻¹) for 1 h. After cooling to -30 °C in the same Ar flow, CO/Ar (10 vol.%, 50 mL min⁻¹) was flowed through the sample at -30 °C for 0.5 h. Finally, the sample was flushed with Ar flow (50 mL min⁻¹) at -30 °C for 0.5 h to remove the physically adsorbed CO on the surface sample. The CO-DRIFTS spectra were obtained by averaging 16 sequentially collected scans at a resolution of 4 cm⁻¹.

In situ CH₄-DRIFTS measurement. For in situ CH₄-DRIFT, 20 mg sample was packed into a Harrick Praying Mantis high-temperature reaction chamber (CaF₂ windows) mounted inside of a Thermo Scientific Praying Mantis diffuse reflectance adapter, set inside of a Thermo Scientific Nicolet 6700 FT-IR spectrometer using liquid nitrogen cooled MCT detector. The sample was pretreated by heating in Ar flow (50 mL min⁻¹) at 400 °C for 1 h and cooled down to 50 °C in the same Ar flow. Gases (5 vol.% CH₄/Ar or Ar) were flowed using Alicat mass flow controllers. The hydrogen peroxide is brought into the chamber by a carrier gas (5 vol.% CH₄/Ar) with a positive pressure (0.15 MPa). Afterward, 5 vol.% CH₄/Ar with the hydrogen peroxide was flowed through the catalyst bed at 50 °C for 0.5 h, followed by flushing with Ar flow (50 mL min⁻¹) for 0.5 h at the same temperature. The in situ CH₄-DRIFTS spectra were obtained by averaging 16 sequentially collected scans at a resolution of 4 cm⁻¹. For CH₄-DRIFTS measurement, all the parameters are the same with in situ CH₄-DRIFTS measurement, except for the absence of H₂O₂.

DFT calculations. All calculations were carried out using DFT implemented in the CASTEP³⁶. The electron exchange and correlation interaction were calculated with the generalized gradient approximation (GGA) in the parametrization of Perdew-Burke-Ernzerhof (PBE) pseudopotentials^{37,38}. To minimize the computational cost for the surface modeling, ultrasoft pseudopotential scheme has been chosen with the cutoff energy of 410 eV^{39,40}. For both SAs Rh-CeO₂ and Rh/CeO₂, the CeO₂ crystal has been cleaved along the (111) plane with three-layer thickness. For SAs Rh-CeO₂ model, only one Rh atom is deposited onto the CeO₂ surface within the unit cell to demonstrate the single-atom catalyst. For Rh/CeO₂ NWs model, the Rh cluster consists of eight atoms, which is cleaved from the bulk Rh crystal along the (111) plane. We imposed a 15 Å vacuum space along z-direction to supply sufficient space for the adsorption behaviors without interactions between lattice. For all the geometry optimizations, the Hellmann-Feynman forces will be converged to <0.001 eV/Å, while the total energy has been converged to 5 × 10⁻⁵ eV per atom. The coarse k-point has been applied for the energy minimization based on the Broyden-Fletcher-Goldfarb-Shannon (BFGS) algorithm^{41,42}.

Data availability

The data supporting this study are available in the paper and Supplementary Information. All other relevant source data are available from the corresponding authors upon reasonable request.

Received: 17 September 2019; Accepted: 15 December 2019;

Published online: 19 February 2020

References

- Wang, V. C. C. et al. Alkane oxidation: methane monooxygenases, related enzymes, and their biomimetics. *Chem. Rev.* **117**, 8574–8621 (2017).
- Shan, J. et al. Mild oxidation of methane to methanol or acetic acid on supported isolated rhodium catalysts. *Nature* **551**, 605–608 (2017).
- Hickman, D. A. & Schmidt, L. D. Production of syngas by direct catalytic oxidation of methane. *Science* **259**, 343–346 (1993).
- Schwach, P., Pan, X. & Bao, X. Direct conversion of methane to value-added chemicals over heterogeneous catalysts: challenges and prospects. *Chem. Rev.* **117**, 8497–8520 (2017).
- Liang, Z. et al. Low-temperature activation of methane on the IrO₂ (110) surface. *Science* **356**, 299–303 (2017).
- Ravi, M., Ranocchiaro, M. & van Bokhoven, J. A. The direct catalytic oxidation of methane to methanol—a critical assessment. *Angew. Chem. Int. Ed.* **56**, 16464–16483 (2017).

- Spivey, J. J. & Hutchings, G. Catalytic aromatization of methane. *Chem. Soc. Rev.* **43**, 792–803 (2014).
- Periana, R. A. et al. Platinum catalysts for the high-yield oxidation of methane to a methanol derivative. *Science* **280**, 560–564 (1998).
- Sushkevich, V. L., Palagin, D. & van Bokhoven, J. A. The effect of the active-site structure on the activity of copper mordenite in the aerobic and anaerobic conversion of methane into methanol. *Angew. Chem. Int. Ed.* **57**, 8906–8910 (2018).
- Agarwal, N. et al. Aqueous Au-Pd colloids catalyze selective CH₄ oxidation to CH₃OH with O₂ under mild conditions. *Science* **358**, 223–227 (2017).
- Yang, X. F. et al. Single-atom catalysts: a new frontier in heterogeneous catalysis. *Acc. Chem. Res.* **46**, 1740–1748 (2013).
- Pelletier, J. D. A. & Basset, J. M. Catalysis by design: well-defined single-site heterogeneous catalysts. *Acc. Chem. Res.* **49**, 664–677 (2016).
- Valden, M., Lai, X. & Goodman, D. W. O. Onset of catalytic activity of gold clusters on titania with the appearance of nonmetallic properties. *Science* **281**, 1647–1650 (1998).
- Huang, W. X. et al. Low-temperature transformation of methane to methanol on Pd₁O₄ single sites anchored on the internal surface of microporous silicate. *Angew. Chem. Int. Ed.* **55**, 13441–13445 (2016).
- Tang, Y. et al. Single rhodium atoms anchored in micropores for efficient transformation of methane under mild conditions. *Nat. Commun.* **9**, 1231 (2018).
- Kwon, Y. et al. Selective activation of methane on single-atom catalyst of rhodium dispersed on zirconia for direct conversion. *J. Am. Chem. Soc.* **139**, 17694–17699 (2017).
- Kyriakou, G. et al. Isolated metal atom geometries as a strategy for selective heterogeneous hydrogenations. *Science* **335**, 1209–1212 (2012).
- Yan, H. et al. Single-atom Pd₁/graphene catalyst achieved by atomic layer deposition: remarkable performance in selective hydrogenation of 1, 3-butadiene. *J. Am. Chem. Soc.* **137**, 10484–10487 (2015).
- Pei, G. X. et al. Ag alloyed Pd single-atom catalysts for efficient selective hydrogenation of acetylene to ethylene in excess ethylene. *ACS Catal.* **5**, 3717–3725 (2015).
- Lucci, F. R. et al. Selective hydrogenation of 1, 3-butadiene on platinum-copper alloys at the single-atom limit. *Nat. Commun.* **6**, 8550 (2015).
- Kim, M. & Laine, R. M. One-step synthesis of core-shell (Ce_{0.7}Zr_{0.3}O₂)_x(Al₂O₃)_{1-x} [(Ce_{0.7}Zr_{0.3}O₂)@Al₂O₃] nanopowders via liquid-feed flame spray pyrolysis (LF-FSP). *J. Am. Chem. Soc.* **131**, 9220–9229 (2009).
- Liu, X. et al. Oxygen vacancy clusters promoting reducibility and activity of ceria nanorods. *J. Am. Chem. Soc.* **131**, 3140–3141 (2009).
- Wang, L. et al. Atomic-level insights in optimizing reaction paths for hydroformylation reaction over Rh/CoO single-atom catalyst. *Nat. Commun.* **7**, 14036 (2016).
- Rice, C. A. et al. The oxidation state of dispersed Rh on Al₂O₃. *J. Chem. Phys.* **74**, 6487–6497 (1981).
- Lang, R. et al. Hydroformylation of olefins by a rhodium single-atom catalyst with activity comparable to RhCl(PPh₃)₃. *Angew. Chem. Int. Ed.* **55**, 16054–16058 (2016).
- Hammond, C. et al. Direct catalytic conversion of methane to methanol in an aqueous medium by using copper-promoted Fe-ZSM-5. *Angew. Chem. Int. Ed.* **51**, 5129–5133 (2012).
- Rosen, G. M. et al. Influence of conformation on the EPR spectrum of 5,5-dimethyl-1-hydroperoxy-1-pyrrolidinyloxy: a spin trapped adduct of superoxide. *J. Org. Chem.* **69**, 1321–1330 (2004).
- Engdahla, A. & Nelander, B. The HOOH-HOO complex. A matrix isolation study. *Phys. Chem. Chem. Phys.* **6**, 730–734 (2004).
- Cai, W. et al. Enhanced catalytic degradation of AO₇ in the CeO₂-H₂O₂ system with Fe³⁺ doping. *Appl. Catal. B: Environ.* **101**, 160–168 (2010).
- Ji, P. et al. Ce³⁺-centric organic pollutant elimination by CeO₂ in the presence of H₂O₂. *ChemCatChem* **2**, 1552–1554 (2010).
- Wang, Y. & Wöll, C. IR spectroscopic investigations of chemical and photochemical reactions on metal oxides: bridging the materials gap. *Chem. Soc. Rev.* **46**, 1875–1932 (2017).
- Wu, Z. et al. Probing the surface sites of CeO₂ nanocrystals with well-defined surface planes via methanol adsorption and desorption. *ACS Catal.* **2**, 2224–2234 (2012).
- Liu, B. et al. Oxygen vacancy promoting dimethyl carbonate synthesis from CO₂ and methanol over Zr-doped CeO₂ nanorods. *ACS Catal.* **8**, 10446–10456 (2018).
- Newton, M. A. et al. Room-temperature carbon monoxide oxidation by oxygen over Pt/Al₂O₃ mediated by reactive platinum carbonates. *Nat. Commun.* **6**, 8675 (2015).
- Graciani, J. et al. Highly active copper-ceria and copper-ceria-titania catalysts for methanol synthesis from CO₂. *Science* **345**, 546–550 (2014).
- Clark, S. J. et al. First principles methods using CASTEP. *Z. Fur Kristallographie* **220**, 567–570 (2005).
- Perdew, J. P., Burke, K. & Ernzerhof, M. Generalized gradient approximation made simple. *Phys. Rev. Lett.* **77**, 3865–3868 (1996).
- Hasnip, P. J. & Pickard, C. J. Electronic energy minimisation with ultrasoft pseudopotentials. *Comput. Phys. Commun.* **174**, 24–29 (2006).
- Vanderbilt, D. Soft self-consistent pseudopotentials in a generalized eigenvalue formalism. *Phys. Rev. B* **41**, 7892–7895 (1990).
- Perdew, J. P. et al. Atoms, molecules, solids, and surfaces: applications of the generalized gradient approximation for exchange and correlation. *Phys. Rev. B* **46**, 6671–6687 (1992).
- Head, J. D. & Zerner, M. C. A Broyden–Fletcher–Goldfarb–Shanno optimization procedure for molecular geometries. *Chem. Phys. Lett.* **122**, 264–270 (1985).
- Probert, M. I. J. & Payne, M. C. Improving the convergence of defect calculations in supercells: an ab initio study of the neutral silicon vacancy. *Phys. Rev. B* **67**, 075204 (2003).

Acknowledgements

This work was financially supported by the Ministry of Science and Technology (2016YFA0204100, 2017YFA0208200), the National Natural Science Foundation of China (21571135), Young Thousand Talented Program, Jiangsu Province Natural Science Fund for Distinguished Young Scholars (BK20170003), the project of scientific and technologic infrastructure of Suzhou (SZS201708), the Priority Academic Program Development of Jiangsu Higher Education Institutions (PAPD), and the start-up supports from Soochow University. The authors thank beamline BL14W1 (Shanghai Synchrotron Radiation Facility) for providing the beam time.

Author contributions

X.H. and Y.X. conceived and supervised the research. X.H., S.B., and Y.X. designed the experiments. X.H., S.B., Y.X., and Q.S. performed most of the experiments and data analysis. J.W. and Fan Li performed and analyzed the STEM characterization. X.H., S.B., Y.X., Q.S., Fangfang Liu, and H.L. participated in various aspects of the experiments and discussions. Fangfang Liu, B.H., H.L., T.W., and M.S. performed the DFT simulations. X.H., S.B., and Y.X. wrote the paper. All authors discussed the results and commented on the paper.

Competing interests

The authors declare no competing interests.

Additional information

Supplementary information is available for this paper at <https://doi.org/10.1038/s41467-020-14742-x>.

Correspondence and requests for materials should be addressed to J.W., Y.X. or X.H.

Peer review information *Nature Communications* thanks the anonymous reviewer(s) for their contribution to the peer review of this work.

Reprints and permission information is available at <http://www.nature.com/reprints>

Publisher's note Springer Nature remains neutral with regard to jurisdictional claims in published maps and institutional affiliations.



Open Access This article is licensed under a Creative Commons Attribution 4.0 International License, which permits use, sharing, adaptation, distribution and reproduction in any medium or format, as long as you give appropriate credit to the original author(s) and the source, provide a link to the Creative Commons license, and indicate if changes were made. The images or other third party material in this article are included in the article's Creative Commons license, unless indicated otherwise in a credit line to the material. If material is not included in the article's Creative Commons license and your intended use is not permitted by statutory regulation or exceeds the permitted use, you will need to obtain permission directly from the copyright holder. To view a copy of this license, visit <http://creativecommons.org/licenses/by/4.0/>.

© The Author(s) 2020